ACS APPLIED MATERIALS & INTERFACES

www.acsami.org

Forum Article

Control of Anisotropy and Magnetic Hyperthermia Effect by Addition of Cobalt on Magnetite Nanoparticles

Adriele Aparecida de Almeida,* Fernando Fabris, Gustavo Soares da Silva, Kleber Roberto Pirota, Marcelo Knobel, and Diego Muraca*

Cite This: https://doi.org/10.1021/acsami.4c03343

Read Online

ACCESS | Metrics & More | Article Recommendations

ABSTRACT: Magnetic hyperthermia (MH) has emerged as a promising technology with diverse applications in medical and technological fields, leveraging the remote induction of temperature elevation through an alternating magnetic field. While Fe_3O_4 nanoparticles with an average size around 12−25 nm are commonly employed in MH systems, this study introduces a strategy to produce smaller particles (less than or equal to 10 nm) with enhanced heating efficiency, as measured by specific power absorption (SPA). We conducted an exhaustive and detailed investigation into the morphological and magnetic properties of $Co_xFe_{3-x}O_4$ nanoparticles, aiming to optimize their MH response. By varying the Co content, we successfully tuned the effective magnetic anisotropy while maintaining saturation magnetization nearly constant. The MH analysis indicates that these nanoparticles predominantly heat through the Néel mechanism, demonstrating robust reproducibility across different concentrations, viscosity mediums, and ac field conditions. Notably, we identified an optimal anisotropy or Co concentration that maximizes SPA, crucial for developing magnetic systems requiring particles with specific sizes. This work contributes to advancing the understanding and application of MH, particularly in tailoring nanoparticle properties for targeted and efficient heat generation in various contexts.

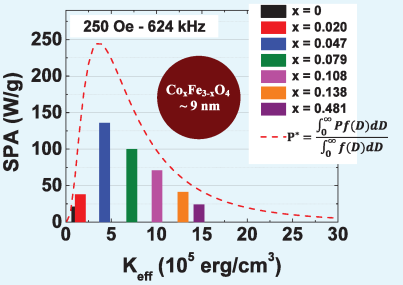

KEYWORDS: *Magnetic hyperthermia, Nanoparticles, Specific power absorption, Magnetic anisotropy, Néel relaxation*

INTRODUCTION

Magnetic hyperthermia (MH) is a technique that involves raising the temperature of a medium by exploiting the magnetic losses exhibited by magnetic nanoparticles when subjected to an alternating current (ac) magnetic field at radiofrequency levels. In this process, the targeted medium, often biological tissues or fluids[1−5] or viscous fluids,[6−8] experiences controlled heating due to the energy dissipation from the magnetic materials. The choice of magnetic nanoparticles provides versatility, and the application of an ac magnetic field in the radiofrequency range allows precise control over the induced heat,[5,9,10] making MH a promising approach in various fields, particularly in targeted medical treatments where controlled and localized heating is advantageous[1−3,5] and, too, to control the viscosity of the petroleum where changing the rheological properties of the petroleum can facilitate its transport.[7,8] Ferrite nanoparticles serve as compelling systems for MH due to the ability to manipulate their magnetic properties through composition and size control.[11,12] Beyond this tunability, they exhibit a plethora of potential applications, adding to their overall significance in various fields.[13] It is important to note that while the hydrophobic nature of the nanoparticles used in this study may limit their direct suitability for biomedical applications, it is worth noting that surface modifications of nanoparticles can be implemented to render these nanoparticles suitable for biomedical uses. It is worth noting that nanoparticles with hydrophobic surfaces exhibit a strong affinity for oil, making them essential for controlling petroleum viscosity, for example. These facts highlight possible versatility across different industrial and medical applications.

In MH of monodomain magnetic nanoparticles (MNPs) within a viscous medium, two main relaxation mechanisms are important: the viscous mechanism (Brown) and the moment inversion mechanism against an energy barrier (Néel).[14] That is, mechanical or Brown mechanism (τ_B) relies on the rheological properties of the system that is given by

$$\tau_B = \frac{3\eta V_{hyd}}{k_B T} \quad (1)$$

where η is the viscosity of the medium, V_{hyd} the hydro dynamic volume of the MNPs, and $k_B T$ the thermal energy. In contrast,

Special Issue: Forum Focused on South American Authors

Received: February 28, 2024
Revised: June 20, 2024
Accepted: June 25, 2024
Published: July 15, 2024

Néel relaxation (τ_N) relies on the magnetic properties of the particles and is expressed by

$$\tau_N = \tau_0 e^{K_{eff} V_{mag}/k_B T} \quad (2)$$

where K_{eff} is the effective magnetic anisotropy, V_{mag} the magnetic volume of the single-domain MNPs, and τ_0 is the characteristic relaxation time (typically between 10^{-9}–10^{-11} s).[14,15] It is known that the dominating relaxation process will be the one with the shorter relaxation time, where the effective relaxation time (τ) is given by[15] $\frac{1}{\tau} = \frac{1}{\tau_N} + \frac{1}{\tau_B}$. The predominance of one mechanism over the other is associated with different intrinsic properties of the particles, such as K_{eff} and V_{mag}, as well as the viscosity of the medium (η) in which they are dispersed, and the V_{hyd} in this medium.[15,16] Furthermore, the heat generation efficiency of MNPs in a hyperthermia experiment, referred to as specific power absorption (SPA), will depend on the parameters of the alternating magnetic field, such as frequency (f) and amplitude (H_0).[15] A nuanced understanding of these factors is essential for a comprehensive grasp of hyperthermia dynamics, offering valuable insights for optimizing its applications.

The key parameter in MH is the SPA of the MNPs and is determined by the magnetic, morphological, and rheological properties of the solvent/MNPs.[15] The SPA is frequently utilized to assess the effectiveness of a MH system in generating heat in target regions.

To maintain experiment reproducibility is important that MNPs intended for hyperthermia applications should be fabricated in a way that favors the dominance of τ_N,[1,6,12,17] as heating efficiency relies solely on the intrinsic magnetic properties of MNPs and remains independent of the variable viscosity in different medium. Additionally, MNPs tend to aggregate when dispersed in some medium.[6,18,19] Under these conditions, the Néel mechanism undergoes changes due to interactions, allowing for the adjustment of magnetics properties to maintain high heating efficiency. Meanwhile, as we saw in the equation above, the Brown relaxation time significantly and inevitably increases, leading to the loss of absorption capability within a reasonable frequency range for efficient hyperthermia application.

The thermal power or power dissipation (P) generated by MNPs under an alternating field, also measured in terms of SPA, can be analytically described by[15]

$$P = \pi \mu_0 \chi_0 H_0^2 f \frac{2\pi f\tau}{1 + (2\pi f\tau)^2} \quad (3)$$

where μ_0 is the permeability in a vacuum. χ_0 is the equilibrium susceptibility defined in the low-field region as $\chi_0 \approx \frac{\mu_0 \rho M_s^2 V_{mag}}{3k_B T}$, where ρ is density and M_s the saturation magnetization of the material.[18,20] This is then an analytical form to calculate the power dissipated by superparamagnetic particles subjected to an external field within the limits of the linear response theory (LRT).[15,17]

Briefly, the thermal power generated by MNPs in the presence of an alternating magnetic field depends on field parameters, specifically its power, and the dissipation related to the ratio between the field frequency and the magnetic moment relaxation time. Therefore, the heat generated by magnetic losses is directly linked to the relaxation mechanisms of the magnetic moment, τ_B and/or τ_N, transforming electromagnetic energy into thermal energy.

In a hyperthermia experiment, the SPA is related to the heating rate through a quick thermodynamic analysis, assuming some factors: first, there are no thermal losses, especially to the surroundings, and second, the mass of MNPs dispersed in the medium is much smaller than the medium. Therefore, it can be expressed as

$$SPA = c_p \frac{m_{medium}}{m_{MNPs}} \frac{\Delta T}{\Delta t} \quad (4)$$

where c_p is the specific heat of the medium, m_{medium} is the mass of the medium, m_{MNPs} is the mass of MNPs, and $\frac{\Delta T}{\Delta t}$ is the heating rate obtained from the initial slope of the heating curve.

Among the various types of MNPs explored for MH, magnetite nanoparticles (Fe_3O_4) emerge as the most extensively investigated due to their favorable magnetic properties, biocompatibility, and cost-effectiveness. However, considering only the Néel relaxation time, an additional complexity arises in optimizing the performance of MNPs. For applications requiring MNPs with a diameter less than or equal to ~10 nm, a reduction in Fe_3O_4 efficiency for MH is observed,[21,22] with an ideal size around 12–25 nm.[21,22] As evidenced in eq 3, considering only the Néel relaxation, adjusting the size of MNPs to achieve an ideal SPA is more challenging than tuning K_{eff}. Given this, we utilized eq 3, for a fixed size of 9 nm (~ average size among the 7 samples this work), and varying K_{eff} from 1×10^5 erg/cm^3 (Fe_3O_4 anisotropy)[23,24] to 20×10^5 erg/cm^3 ($Co_1Fe_2O_4$ anisotropy)[24−27] we can calculate the expected P values, as depicted in the graph of Figure 1. We observed that to achieve optimal

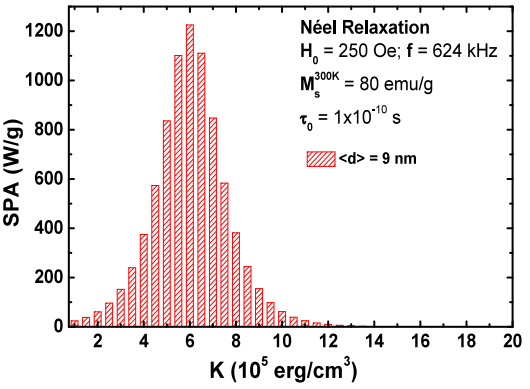

Figure 1. Estimated power dissipation as a function of magnetic anisotropy obtained using eq 3 and considering exclusively the Néel relaxation time. The magnetic parameters used in the equation are cited in the graph.

efficiency in MH with MNPs of diameter less than 10 nm, heating through the Néel mechanism, it is crucial to increase the anisotropy of Fe_3O_4.

Previous studies have explored doping magnetite with Co to modulate heat absorption in magnetic hyperthermia.[28−30] However, the coprecipitation synthesis method used resulted in increased nanoparticle size and decreased magnetic saturation with higher cobalt content,[29,30] limiting precise control over size and magnetic anisotropy. Conversely, Fantechi et al.[28] synthesized $Co_xFe_{3-x}O_4$ particles via thermal

https://doi.org/10.1021/acsami.4c03343
ACS Appl. Mater. Interfaces XXXX, XXX, XXX−XXX

Table 1. Chemistry and Structural Results Obtained for All $Co_xFe_{3-x}O_4$ Samples[a]

$Co_xFe_{3-x}O_4$sample name	Nominal stoichiometry	TXRF stoichiometry	$\langle d\rangle_{XRD}$ (nm)	$\langle d\rangle_{TEM}$ (nm)	σ_{TEM}
$x = 0$	Fe_3O_4	Fe_3O_4	9.7	7.9	0.2
$x = 0.020$	$Co_{0.02}Fe_{2.98}O_4$	$Co_{0.020}Fe_{2.980}O_4$	8.5	8.4	0.2
$x = 0.047$	$Co_{0.04}Fe_{2.96}O_4$	$Co_{0.047}Fe_{2.953}O_4$	12	10.6	0.4
$x = 0.079$	$Co_{0.06}Fe_{2.94}O_4$	$Co_{0.079}Fe_{2.921}O_4$	11	9.4	0.3
$x = 0.108$	$Co_{0.08}Fe_{2.92}O_4$	$Co_{0.108}Fe_{2.892}O_4$	9.9	8.1	0.3
$x = 0.134$	$Co_{0.1}Fe_{2.9}O_4$	$Co_{0.134}Fe_{2.866}O_4$	9.5	8.7	0.3
$x = 0.481$	$Co_{0.5}Fe_{2.5}O_4$	$Co_{0.481}Fe_{2.519}O_4$	9.1	9.1	0.2

[a]Given sample names, nominal stoichiometry, the stoichiometry obtained by TXRF analysis, average diameter $\langle d\rangle_{XRD}$ obtained from XRD pattern, and average diameter $\langle d\rangle_{TEM}$ and size dispersion (σ_{TEM}) obtained from the TEM images analyzes.

decomposition of acetylacetonates, achieving an average size of around 8 nm with varying x from 0 to 1. They reported an unexpected reduction in magnetic anisotropy for $x > 0.6$ and maximum heat absorption at $x = 0.6$.

In this study, we delved into the impact of varying the Co content on the MH properties of cobalt ferrite $Co_xFe_{3-x}O_4$ type nanoparticles. As the value of x increased from 0 to 0.481 in particles with an average size of around 9 nm, we observed a continuously increase in K_{eff}. MH assessments conducted in two distinct media, one with low[31] and the other with high[6,32] viscosity (η), revealed similar SPA values, indicating that MNPs predominantly undergo heating through the Néel relaxation mechanism. Notably, the SPA values exhibited a clear dependence on K_{eff}, allowing us to pinpoint an optimal SPA for a specific particle size with $x = 0.047$.

MATERIALS AND METHODS

$Co_xFe_{3-x}O_4$ oleic acid-coated MNPs reported here were obtained by high temperature thermal decomposition of the Fe(III) and Co(II) acetylacetonates (6 mMol totals/together) dispersed in 120 mMol of benzyl ether solvent, 6 mMol of 1,2-octanediol, oleic acid (9 mMol), and oleylamine (9 mMol) (surfactants). Stoichiometry of each sample was controlled by the acetylacetonates ratio used in the solution from where different compositions were obtained (see Table 1). For all samples, the solution was heated between ∼100−120 °C during 20 min under N_2 flow and intense mechanical stirring. After that, N_2 was removed, and the solution was slowly heated until the reflux condition (298 °C) with a heating rate of 3 °C/min. The solution was kept in reflux during 60 min.

The chemical composition of the samples was determined by total reflection X-ray fluorescence (TXRF) measurements, with a S4 T-STAR Bruker equipped with a Mo X-ray source. In the TXRF procedure, powdered samples were adhered to sample holders using a drop of each sample dispersed in a mixture of hexane and water. Measurements were carried out postevaporation of hexane and water. Structural characterization was carried out using a X-ray diffraction (XRD) measurements with D2 Phaser diffractometer (Bruker) using Cu Kα radiation (λ = 1.5418 A°), operating at 30 kV and 10 mA, in the 2θ range from 25° to 90° with steps of 0.02° at room-temperature. Samples were cleaned with acetone to remove organic material, and the powder was deposited in the sample holder. The size, diameter dispersion, and high-resolution (HRTEM) analysis of our MNPs were conducted using transmission electron microscopy (TEM) on a JEOL JEM 2100F, operating at 200 kV. For the microscopy experiment, samples were dispersed in toluene and then prepared by drying a drop of the suspension on a Ted Pella ultrathin cooper film on a holey carbon. The diameter histogram was generated by measuring the diameter of at least ∼400 MNPs, and the average diameter ($\langle d\rangle$) and dispersion (σ) were determined by fitting the data with a log-normal distribution.

Percentage of organic compound in the nanoparticles to have accuracy in mass to normalize magnetization experimental data with the oxide amount was determined for each sample by means of differential thermal thermogravimetric analyzer (TGA), model 2950 TGA HR V5.3C. Samples powder was heating up to 1000 °C with a heating rate of 5 °C/min in Ar flux (60 mL/min) while weight was measured. This analysis revealed that approximately 10−15% of the total mass in all samples consisted of organic compounds. This fraction of organic material in the MNPs was subsequently subtracted from the overall sample mass during magnetic measurements. The magnetic characterization needed in order to understand the MNPs response in MH experiments are the M_s, the K_{eff} constant, and blocking temperature (T_B). M_s and K_{eff} were determined by magnetization measurements as a function of the applied field ($M(H)$) measured at various temperatures. Blocking temperature distribution ($f(T_B)$) of each sample was obtained from the magnetization curves as a function of temperature ($M(T)$) measured in the zero-field-cooling and field-cooling modes (ZFC and FC curves, respectively) by[6] $f(T_B) \sim \left(\frac{1}{T}\right)\frac{d(M_{ZFC} - M_{FC})}{dT}$. The average value of the T_B ($\langle T_B\rangle$) was calculated from the Kloster et al. reference.[33] These magnetic measurements were performed in a commercial SQUID magnetometer (Quantum Design, MPMS3), and the samples were conditioned by dispersing the MNPs in epoxy resin (∼0.03 wt %), avoiding the agglomeration and physical rotation of the nanoparticles.

For the magnetic hyperthermia experiments, the MNPs were dispersed in paraffin and toluene at a controlled concentration and performed in two different commercial models (nB nanoScale Biomagnetics company D5 Series model from Spain and Fives company Celes MP 6 kW from France), with a working amplitude of 200−600 Oe and frequency of 250−624 kHz.

To avoid any effects of dipolar interactions all magnetic measures as well as specific absorption rate or calorimetric properties were done in a very low nanoparticles concentration, guaranteeing a strong dispersion of them.

RESULTS AND DISCUSSION

In order to tune magnetic properties of the $Co_xFe_{3-x}O_4$ samples, the chemical composition of obtained MNPs is of great importance, since the magneto-hyperthermia properties strongly determined them. To enhance SPA in nanoparticles with a size around 9 nm, the ratio of Fe and Co in the ferrite nanoparticles was altered, changing the magnitude of the internal magnetic moment due to the presence of the ion Co. But in the composition range we are working, the most significant effect should be changes on effective anisotropy constant of the system, K_{eff}, and to a lesser degree on saturation magnetization, M_s, as we will see in the magnetic results below.

The effective stoichiometry of each resulting sample was determined using TXRF (presented in Table 1). From the table, we see that the amount of Co in the final stoichiometry of the MNPs is not the same molar ratio expected from the amount of the precursors used in the synthesis; however, it is very close to what was expected.

Room temperature XRD of all the samples synthesized, with different cobalt concentrations, are shown in Figure 2. The

https://doi.org/10.1021/acsami.4c03343
ACS Appl. Mater. Interfaces XXXX, XXX, XXX−XXX

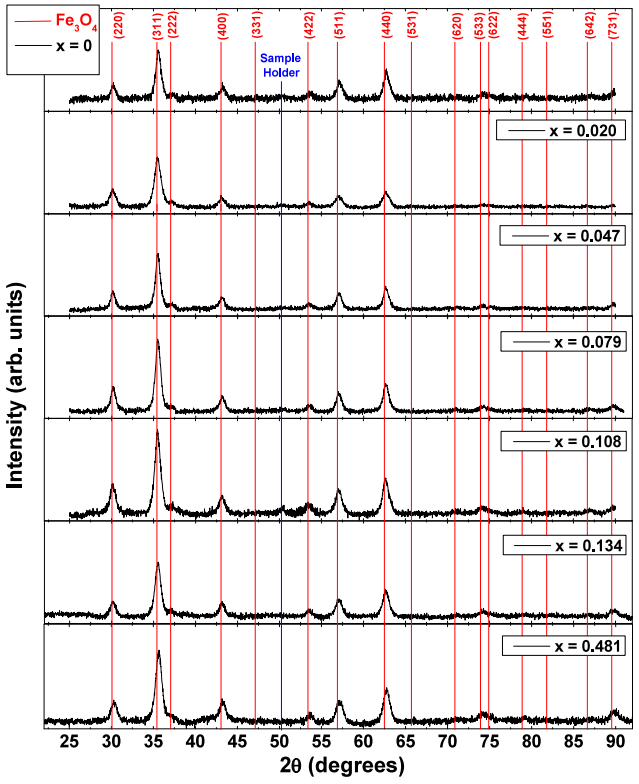

Figure 2. XRD pattern of the $Co_xFe_{3-x}O_4$ samples. All peaks are indexed with the magnetite where the red bars correspond to the diffraction peaks according to the COD number 1010369 (Fe_3O_4). The blue bar, in ~50.1°, corresponds to a peak from the glass sample holder.

crystalline phase of the samples contains strong diffraction peaks at 2θ = 30.2°, 35.5°, 43.2°, 53.5°, 57.1°, and 62.8°, corresponding to (220), (311), (400), (422), (511), and (440) crystalline planes of cubic magnetite phase, respectively (COD number 1010369). The average crystallite diameter $\left(\langle d\rangle_{\mathrm{XRD}} = \frac{0.9\lambda}{\beta \cos \theta_{\mathrm{DRX}}}\right)$ was calculated according to the Scherrer's equation, where it was considered as 0.9 shape parameter in the Scherrer equation,[34] λ is the wavelength of the X-ray (Cu Kα, λ = 1.5418 $A°$), β is the full-width at half-maximum (fwhm) of the diffraction peak studied, and θ_{XRD} the Bragg angle. With a pseudo-Voigt fit (linear combination of the Gaussian and Lorentzian function) on the peak [113] of Figure 2, the value of the fwhm is obtained and, consequently, an average crystallite size for all samples and is found in Table 1. Using the Scherrer's equation is very close to the data of TEM images.

Morphology and size of the magnetic nanoparticles were studied using the TEM, and analysis shows that $Co_xFe_{3-x}O_4$ MNPs prepared by the thermal decomposition method have good narrow size distribution. Figure 3 shows representative TEM images from $Co_xFe_{3-x}O_4$ nanoparticles, sizes 7.9−10.6 nm, deposited from their hexane suspension and dried under ambient conditions. The respective diameter histograms are presented in the respective right panels and was built up by considering more than 400 nanoparticles on the analysis. Results were fitted using a log-normal distribution for all samples (presenting a dispersion of at most σ_{TEM} ~ 0.4). The values of $\langle d\rangle_{\mathrm{TEM}}$ obtained from the fitting too are given in Table 1. 0.1% of the x = 0.047 sample have MNPs of sizes near

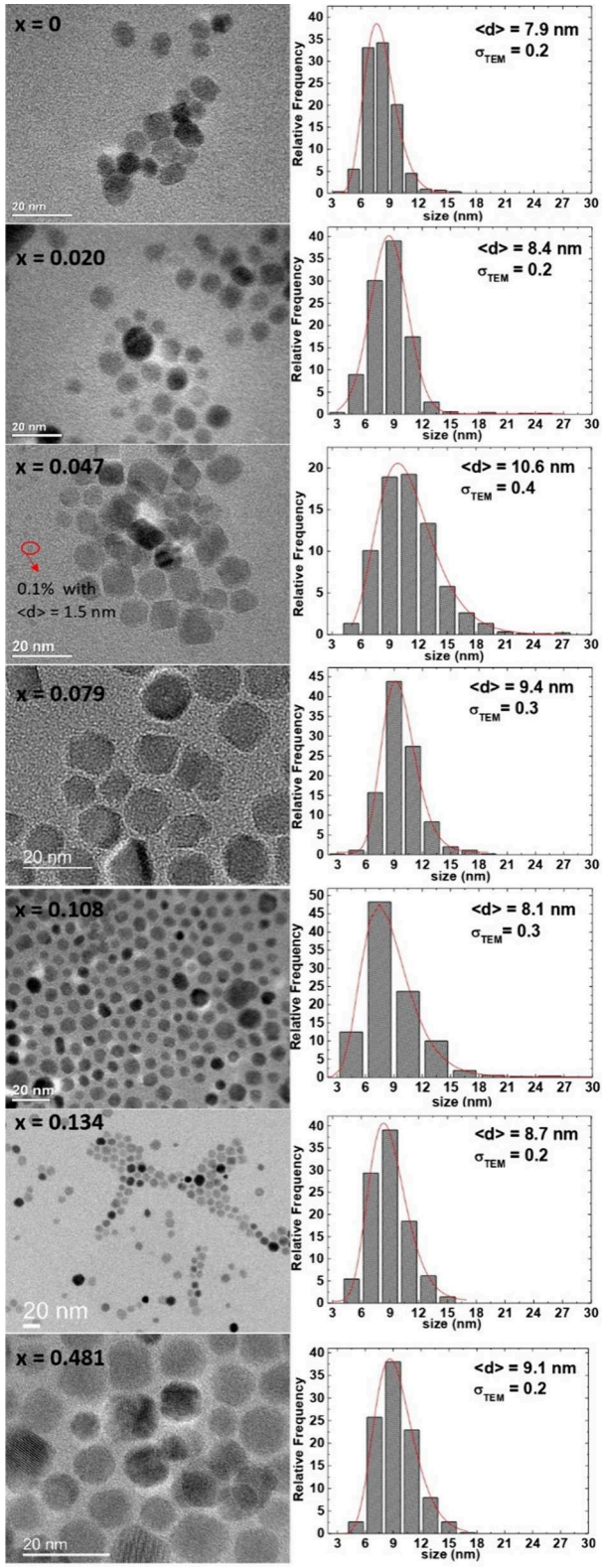

Figure 3. Representative TEM bright field images of $Co_xFe_{3-x}O_4$ nanoparticles obtained by thermal decomposition method and deposited from their hexane dispersion on an amorphous carbon-coated copper grid and dried at room temperature. The right panel shows the respective diameter histograms fitted with a log-normal distribution, whose parameters are given in the figure and Table 1.

1.5 nm; however, the larger ones are the ones that most contribute to the result because of the relative height amount

https://doi.org/10.1021/acsami.4c03343
ACS Appl. Mater. Interfaces XXXX, XXX, XXX−XXX

of magnetic moment when compared with the 0.1% of 1.5 nm nanoparticles.

Figure 4A shows the structural information on a single nanoparticle from the x = 0.079 sample, which was obtained

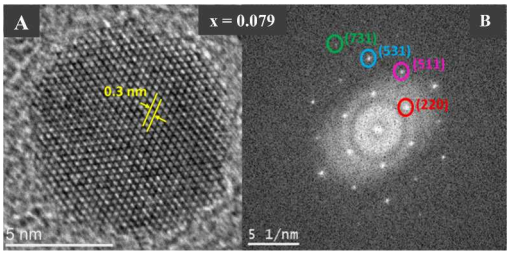

Figure 4. (A) High-resolution TEM image of a single 9.5 nm x = 0.079 nanoparticle where the distance of the crystalline planes equivalent to 0.3 nm is seen. (B) Fourier Transform (FFT) of the same nanoparticle; the FFT patterns are indexed with the cubic spinel interplanar distances, magnetite. (Patterns as indicated by the circles of each color.)

using HRTEM. The distance between the crystalline planes of this nanoparticle is 0.3 nm, corresponding to (220) planes in the spinel-structured magnetite (Fe_3O_4). The nanoparticle in this figure is a single crystal, as it corresponds to the group of atomic planes of Fe_3O_4. The respective Fourier Transform (FFT) pattern of Figure 4B were obtained by processing image Figure 4A using the Gatan software. The measured lattice spacing based on the rings in the FFT pattern are compared with the known lattice spacing for bulk Fe_3O_4, and the found values of [hkl], detailed in the figure, are equivalent to the crystal planes (220), (511), (531), and (731) according to database COD number 1010369.

The $\langle d\rangle_{TEM}$ of samples exhibits good agreement with average particle diameter $\langle d\rangle_{XRD}$ obtained from XRD (Table 1), indicating that each individual particle is a single crystal. Hence, from both TEM and XRD results, we conclude that the $Co_xFe_{3-x}O_4$ nanoparticles with uniform size distribution were successfully fabricated using the thermal decomposition method. From now, the grain size $\langle d\rangle_{TEM}$ will be used instead of crystal and/or particle size in the following heating and magnetic analysis and discussion.

Also from TEM analyses we corroborate that the morphological characteristics of the nanoparticles remain strongly similar across all samples, despite variations in Co concentration, that implies that the relaxation time and, consequently, SPA will primarily hinge on the modification of K_{eff} brought about by the introduction of Co.

Extensive studies were conducted to determine the magnetic anisotropy of each sample. $M(T)$ curves were measured using ZFC and FC protocols with a dc field of H = 50 Oe, as illustrated in Figure 5. The $M(T)$ plots offer insights into the distribution of blocking temperatures $f(T_B)$, where T_B represents the temperature distinguishing between superparamagnetic and blocked regimes within a specific measurement time (approximately 100 s in our case). For a noninteracting monodomain magnetic nanoparticles, the $f(T_B)$ distribution can be obtained by making[6] $\left(\frac{1}{T}\right)\frac{d(M_{ZFC}-M_{FC})}{dT}$. The $f(T_B)$ distribution for each sample is illustrated in Figure 5 (blue lines). By computing the weighted average and its standard deviation of $f(T_B)$, the $\langle T_B\rangle$ and the normalized blocking temperature deviation (σ_{T_B}) was obtained

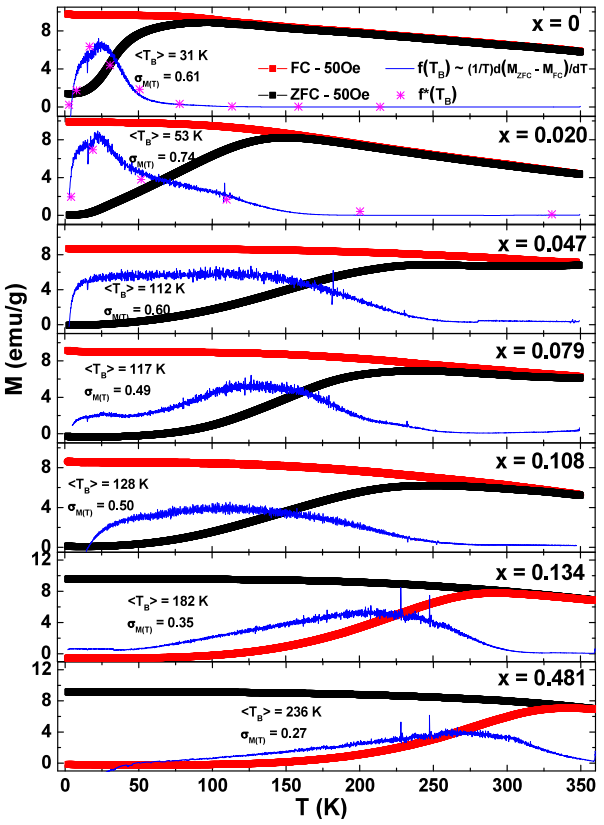

Figure 5. $M(T)$ all the samples $Co_xFe_{3-x}O_4$ measurements in ZFC and FC protocols with applied field of H = 50 Oe. The blocking temperature distributions $f(T_B)$ were calculated for each sample as $\left(\frac{1}{T}\right)\frac{d(M_{ZFC}-M_{FC})}{dT}$ (blue line), and $f^*(T_B)$ was also calculated using the size distribution of the TEM (pink dotted).

and reported in Figure 5. Utilizing the assumption of a uniaxial anisotropy barrier described by $K_{eff}V$, the mean blocking temperatures are often expressed as $\langle T_B\rangle \approx \frac{K_{eff}V}{25k_B}$, with k_B representing the Boltzmann constant.[35] The $\langle T_B\rangle$ values obtained from the $M(T)$ measurements, along with V calculated from the average size obtained by TEM, were used to derive the K_{eff} for each sample, as presented in Table 2. It is worth mentioning here that a relationship between K_{eff} and temperature has previously been established,[36] wherein our calculations of K_{eff} are specifically tied to the average blocking temperature $\langle T_B\rangle$ of each sample. The most significant expected effect of the incorporation of Co in the samples for this work is the change of the K_{eff}. It is noteworthy that the obtained σ_{T_B} from the $M(T)$ analysis is nearly three times the values of σ_{TEM} obtained from TEM, as expected, since σ_{T_B} is a volumetric quantity and needs to be three times larger than the one-dimensional quantity σ_{TEM}. For comparison, $f^*(T_B)$ for the sample x = 0 and x = 0.020 was calculated with the Néel-Brown model (Figure 5, pink dotted) from the size distributions presented in the diameter histogram shown in Figure 3 and assuming a value of $\tau_0 = 10^{-10}$ s, a measurement time τ_m = 100 s, and using the amplitude and uniaxial energy barrier as fit parameters. The calculations were not carried out for the other samples due to the scarcity of data points in the temperature range from 2 to 350 K; this would require a significantly larger count of particle sizes. These results indicate that, at least for the x = 0 and x = 0.020

https://doi.org/10.1021/acsami.4c03343
ACS Appl. Mater. Interfaces XXXX, XXX, XXX−XXX

Table 2. Magnetic Parameters Obtained from $M(T)$ and $M(H)$ Analysis for All $Co_xFe_{3-x}O_4$ Samples[a]

$Co_xFe_{3-x}O_4$ sample name	K_{eff} 10^5 (erg/cm^3) from $M(T)$	$\sigma_{M(T)}$	$M_s(0)$ (emu/g)	α	K_{eff} 10^5 (erg/cm^3) from $\frac{M_r(T)}{M_s}$	$\sigma_{M_r(T)/M_s}$	K_{eff} 10^5 (erg/cm^3) from $H_C(T)$	σ_{H_C}
x = 0	4.1	0.61	91.8 ± 0.5	0.29 ± 0.01	1.2 ± 0.1	0.87 ± 0.02	3.1 ± 0.7	0.9 ± 0.2
x = 0.020	5.9	0.74	100 ± 1	0.40 ± 0.01	1.6 ± 0.2	0.69 ± 0.02	4.2 ± 0.2	0.9 ± 0.2
x = 0.047	6.2	0.60	92.6 ± 0.4	0.69 ± 0.02	4.3 ± 0.3	0.54 ± 0.02	–	–
x = 0.079	10.1	0.49	92.5 ± 0.6	0.68 ± 0.02	7.2 ± 0.4	0.45 ± 0.01	–	–
x = 0.108	15.9	0.50	94.0 ± 0.5	0.71 ± 0.02	10.0 ± 0.6	0.51 ± 0.01	–	–
x = 0.134	18.2	0.35	91.7 ± 0.6	0.78 ± 0.01	12.9 ± 0.5	0.39 ± 0.01	–	–
x = 0.481	20.6	0.27	92.3 ± 0.4	0.81 ± 0.02	14.7 ± 0.5	0.33 ± 0.01	–	–

[a] K_{eff} and $\sigma_{M(T)}$ is the anisotropy obtained from the $M(T)$ analysis; $M_s(0)$ is the saturation magnetization at 0 K obtained of the $M_s(T)$ analysis; α, K_{eff} and $\sigma_{M_r(T)/M_s}$ is the anisotropy obtained from the $\frac{M_r(T)}{M_s}$ analysis; and K_{eff} and σ_{H_c} is the anisotropy obtained from the $H_c(T)$ analysis.

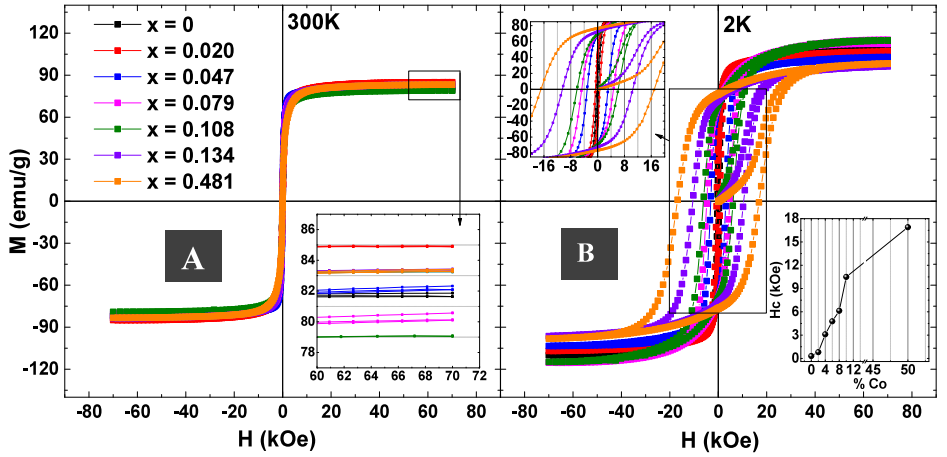

Figure 6. $M(H)$ all samples $Co_xFe_{3-x}O_4$ (A) at temperature of 300 K, with the inset showing a zoom in of the M_s, and (B) at temperature of 2 K, with the inset showing a zoom in of the H_c and the evolution H_c with the Co content.

samples, only the size distribution contributes to the T_B dispersion, and therefore, the compositions of particles are nearly homogeneous.

The $M(H)$ at different temperatures was collected in applied magnetization loops with a maximum field of ±70 kOe for all samples. $M(H)$ at different temperatures, provide information on temperature-dependence of magnetic coercivity (H_c), M_s, and squareness ratio $\left(\frac{M_r(T)}{M_s}\right)$, were M_r is remanence magnetization at 0 Oe, of the samples. Figure 6A, B shows magnetization loops for all samples at 300 and 2 K respectively. Our results show that M_s remains almost unchanged at 300 K, with the increase in the Co content in the ferrite, showing very close values and a variation of only ∼6 emu/g between samples. The insets in Figure 6B show the systematic increase of H_c with increasing Co.[37,38] This increase is closely related to the change in K_{eff},[30] as will be discussed in more detail below.

As a representation for all samples, Figure 7A shows $M(H)$ measurements of sample x = 0.108 performed at different temperatures and how H_c and M_s is strongly temperature dependence. Figure 7B provides a careful analysis of M_s as a function of temperature ($M_s(T)$) with two distinct dependencies observed: one at high temperatures (above ∼50 K) and another at low temperatures (below ∼50 K). Phenomenological models and experimental studies attributed these two components to the temperature dependence of surface and core magnetization. Previous works have reported an exponential-like decrease in surface spin magnetization with increasing temperature and a Bloch $T^{3/2}$ dependence for core magnetization.[39−41] Then, the temperature-dependent magnetization, $M_s(T)$ can be equated as

$$\frac{M_s(T)}{M_s(0)} = (1 - BT^{3/2}) + Ae^{-T/T_f} \quad (5)$$

where B represents the Bloch constant, T_f is the spin freezing temperature, and A denotes the surface spin contribution to $M_s(T)$. This equation was employed to model the experimental $M_s(T)$ curves for all samples. The obtained $M_s(0)$ values, presented in Table 2, align with expectations for Fe_3O_4. Notably, $M_s(0)$ exhibited minimal change with varying Co content. All fits yielded similar values for B and A, where $\tilde{B}(2.5 \pm 0.5) \times 10^{-5}K^{2/3}$ and $\tilde{A}(0.17 \pm 0.07)$. The T_f values obtained ranged from 3 to 30 K, consistent with findings from previous studies.[39,41]

To obtain insights about the Co effects on magnetic anisotropy and its distribution within the samples, M_r and M_s ratios were analyzed (Figure 7C). At 2 K, the $\frac{M_r}{M_s}$ values change from 0.29 to 0.81 depending on Co concentration. The Stoner−Wohlfarth theory predicts, for noninteracting random nanoparticles at 0 K with uniaxial anisotropy, $\frac{M_r}{M_s} = 0.48$, and for cubic anisotropy, $\frac{M_r}{M_s} = 0.83$.[42−44] As the temperature increases, some particles transition to the superparamagnetic state, rendering $\frac{M_r}{M_s} = 0$ for these particles. The temperature-

https://doi.org/10.1021/acsami.4c03343
ACS Appl. Mater. Interfaces XXXX, XXX, XXX−XXX

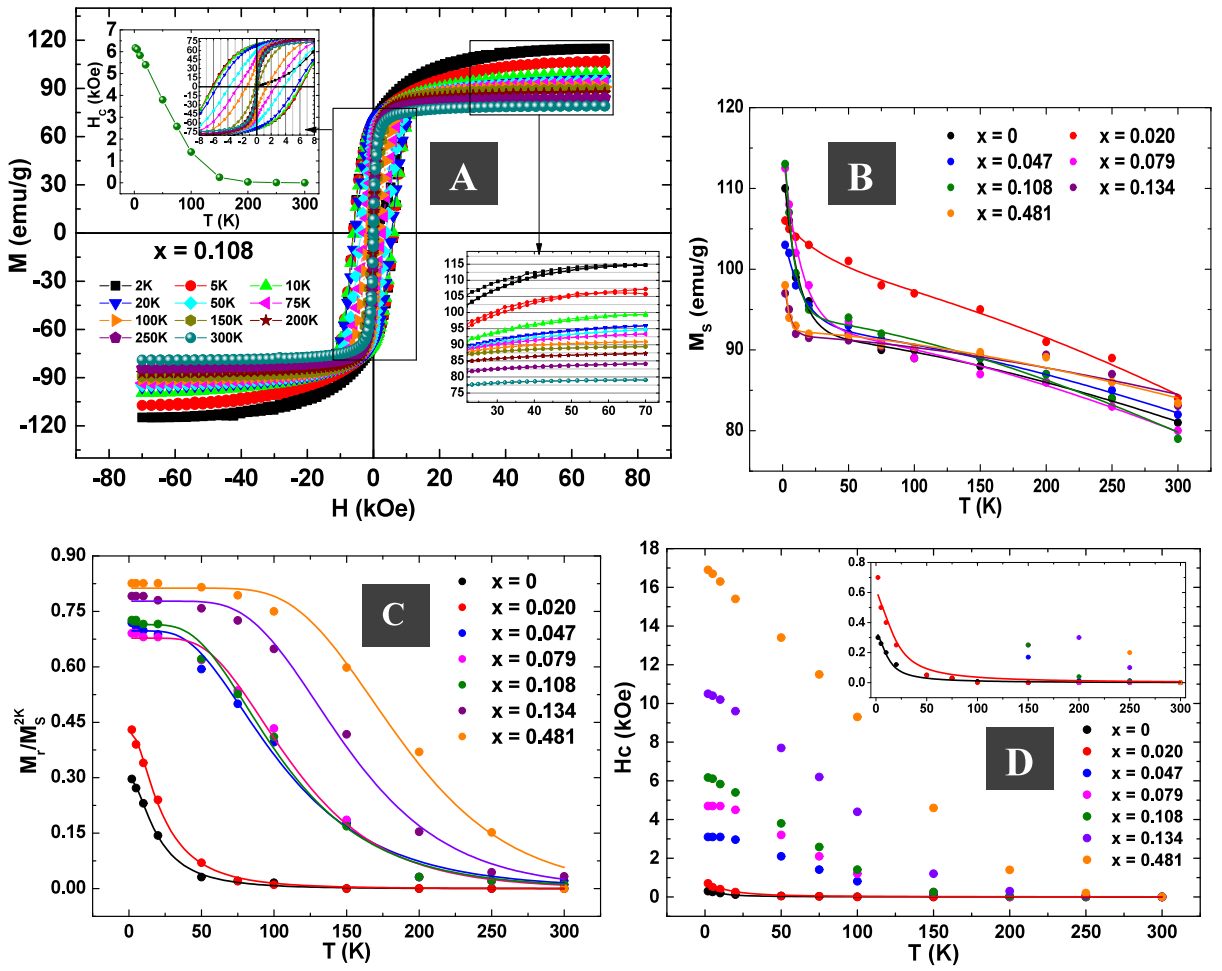

Figure 7. (A) $M(H)$ for sample $x = 0.108$ at different temperatures, M_s and H_c dependence on temperature for this sample is presented in the inset. (B) M_s dependence on temperature ($M_s(T)$), (C) $\frac{M_R}{M_s^{2K}}$ dependence on temperature $\left(\frac{M_R}{M_s^{2K}}(T)\right)$, and (D) H_c dependence on temperature $H_c(T)$ for all the samples $Co_xFe_{3-x}O_4$ nanoparticles, fitting details, the sample $x = 0$ and $x = 0.020$ is presented in the inset.

dependence of $\frac{M_r(T)}{M_s}$ is contingent upon the fraction of particles in the blocked state, expressed by

$$\frac{M_r(T)}{M_s} = \alpha \frac{\int_T^\infty f(T_B)dT}{\int_0^\infty f(T_B)dT} \quad (6)$$

where $\alpha = \frac{M_r(0)}{M_s}$. It is worth mentioning that, unlike the $M(T)$ analyses, the equation above does not assume that the particles present uniaxial anisotropy. On the contrary, information can be obtained about which type of anisotropy are dominant. However, once again, this anisotropy is inherently tied to the temperature $\langle T_B \rangle$, as it serves as the basis for calculating K_{eff}. Experimental data for all samples in Figure 7C were fitted using eq 6, and the obtained α is reported in Table 2. The values of α below 0.5 for the $x = 0$ and $x = 0.020$ samples are in concordance with uniaxial anisotropy.[44] While an α value below 0.5 might seem unconventional, it could be attributed to a number of smaller nanoparticles still unblocked at 2 K, distorting the fitting for these samples.[44] Conversely, for other samples, as Co concentration increases, α approaches a value near 0.75, indicating a relevant cubic magnetocrystalline anisotropy contribution for these samples.[42−44] Hence two contributions to the magnetic anisotropy need to be considered: one from magnetocrystalline anisotropy, presenting cubic anisotropy for both Fe_3O_4 and $CoFe_3O_4$, and another from surface anisotropy, which is uniaxial and can be significant for small particles like ours. For low Co content, the magnetocrystalline contribution is relatively small, with uniaxial surface anisotropy prevailing. However, as the Co content increases, cubic magnetocrystalline anisotropy takes precedence. The decrease $\frac{M_r}{M_s}$ for each curve with increasing temperature is also related to the reduction of the effective magnetic anisotropy force.[42−44]

Concurrently, the temperature-dependent $\frac{M_r(T)}{M_s}$ allows us to deduce the distribution of blocking temperatures for each sample and, consequently, the effective magnetic anisotropy (K_{eff}), as listed in Table 2. The K_{eff} values obtained from the $\frac{M_r(T)}{M_s}$ analysis are slightly larger than those obtained from the analysis of $M(T)$ curves; however, both exhibit the same trend with the increase in Co concentration in the samples.

Additionally, K_{eff} can be determined by fitting the $H_c(T)$ curves, as outlined in the referenced papers.[35,45,46] According to these works, the temperature dependence of the coercive field can be described by

https://doi.org/10.1021/acsami.4c03343
ACS Appl. Mater. Interfaces XXXX, XXX, XXX−XXX

$$H_c(T) = \frac{M_r(T)}{\chi_{SP}(T) + \frac{M_r(T)}{H_{cB}(T)}} \quad (7)$$

where $M_r(T)$ is given by eq 6, $\chi_{SP}(T) = \frac{25M_s^2}{3K_{eff}} \frac{\int_0^T T_B f(T_B)dT}{\int_0^\infty f(T_B)dT}$ is the susceptibility of the fraction of superparamagnetic MNPs, $H_{cB}(T) = \alpha \frac{2K_{eff}}{M_s}\left(1 - \left(\frac{T}{\langle T_B\rangle_T}\right)^{0.5}\right)$ is the coercitive field related only to the blocked NPs at temperature T and $\langle T_B\rangle_T = \frac{\int_T^\infty T_B f(T_B)dT}{\int_T^\infty f(T_B)dT}$ is the average blocking temperature, which takes into account only the volume fraction of blocked particles at temperature T. This model can describe well experimental $H_c(T)$ curves for samples with small amounts of Co; however, it does not fit well for other samples. The curve fittings are shown in Figure 4D for the samples with $x = 0$ and $x = 0.020$, respectively, and the corresponding values of K_{eff} and σ_{H_c} are presented in Table 2. The obtained values for the anisotropy distribution in this analysis agree with those obtained in the $M(T)$ analysis for these samples. It is worth mentioning that this model assumes a uniaxial anisotropy for the energy barrier, limiting its applicability to samples with a small amount of Co, specifically, the two samples exhibiting uniaxial anisotropy ($x = 0$ and $x = 0.020$), as depicted in Figure 7D. Moreover, the resultant temperature-dependent K_{eff} values are directly linked to the adjusted $\langle T_B\rangle$, further emphasizing their temperature dependence.

Hyperthermia tests were conducted on a magnetic fluid sample ($x = 0.108$) in both toluene (low viscosity) and paraffin (high viscosity) at concentrations ranging from 0.5 to 5.2 mg/mL. The results, depicted in Figure 8, were obtained using an ac field with an amplitude of 560 Oe and a frequency of 103 kHz and performer in Celes MP 6 kW model. The SPA values were determined across different concentrations, ranging between 24 and 31 W/g. These values remain unaffected at varying concentrations and even in the presence of significantly different viscosities in the media, from where can be inferred absence of relevant dipolar interaction among the nanoparticles. Furthermore, Néel relaxation as the primary relaxation mechanism for this sample is evident, for example, in paraffin, where the high viscosity hinders the physical movement of nanoparticles, and the results compared with toluene were equal. As the results do not differ from paraffin to toluene, we concluded that the dominant relaxation mechanism is the Néel for the different samples in toluene and paraffin.

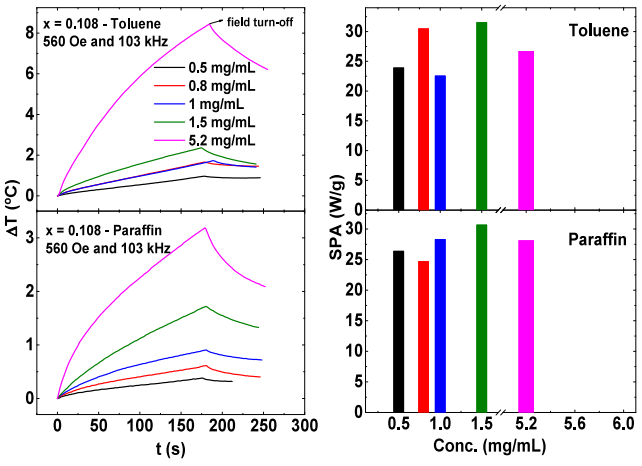

Figure 8. On the left side, MH experiments of magnetic nanoparticles dispersed in toluene (low viscosity) and paraffin (high viscosity) performed in Celes MP 6 kW. The measurements were performed with an ac field of amplitude 560 Oe and frequency 103 kHz for the sample $x = 0.108$ in different concentrations. On the right are their respective values of SPA in toluene and paraffin for each concentration.

A representation of the MH measurements and results of SPA, in paraffin, for all samples are presented in Figure 9. The corresponding SPA values obtained for each sample show a clear dependence on the magnetic anisotropy. Notably, excellent SPA values were achieved, reaching around 200 W/g for the sample with $x = 0.047$ under conditions of 600 Oe and 303 kHz, specifically tailored for particles with an average size of approximately 9 nm.

To validate the obtained SPA values, we estimated the expected SPA by assuming a size distribution and considering only Néel relaxation as the contributing factor. The integration of eq 3 over the size distribution led to the calculated SPA, denoted as P^*:

$$P^* = \frac{\int_0^\infty Pf(D)\,dD}{\int_0^\infty f(D)\,dD} \quad (8)$$

For this estimation, we employed a log-normal distribution with an average size of 9 nm and a size distribution of 0.27, consistent with the TEM results. Obtained P^* values, as a function of K_{eff} for the corresponding field amplitudes and frequencies, are depicted as red dashed lines in Figure 9. These theoretical values match K_{eff} dependence with the experimental SPA results, affirming that the samples solely undergo Néel relaxation and that we can successfully modulate SPA by altering the magnetic anisotropy, as expected, even knowing that eq 8 is only valid for cases where the anisotropy is uniaxial.

Figure 10 presents the outcomes of MH experiments for all samples dispersed in paraffin at a concentration of 5 mg/mL. The measurements were conducted across different field amplitudes and frequencies, revealing distinct heating rates attributed to varying effective magnetic anisotropies. For all explored frequencies and ac field amplitudes, the evolution of SPA with Co concentration exhibits a distinct maximum within the concentration range of $0.020 < x < 0.079$. At the highest frequency of 624 kHz, SPA values escalate from 20.7 W/g ($x = 0$) to 135.7 W/g ($x = 0.047$) before receding to 23.9 W/g ($x = 0.481$). These results underscore the adjustability of K_{eff} to optimize SPA values under different experimental conditions.

CONCLUSION

In this study, we investigated the effects of composition and magnetism on the magnetic hyperthermia response of $Co_xFe_{3-x}O_4$ nanoparticles. We have successfully optimized the SPA, by producing MNPs smaller than 10 nm and through the Néel mechanism, for MH applications. Through a detailed exploration of the morphological and magnetic properties of the nanoparticles, we were able to tune the K_{eff} by varying the Co content in the samples while keeping the M_s and $\langle d\rangle$ relatively constant. This study identified an optimal Co concentration ($x = 0.047$) and/or anisotropy ($K_{eff} = 4.3 \times 10^5$ erg/cm^3) that maximizes SPA (with highest heating

https://doi.org/10.1021/acsami.4c03343
ACS Appl. Mater. Interfaces XXXX, XXX, XXX−XXX

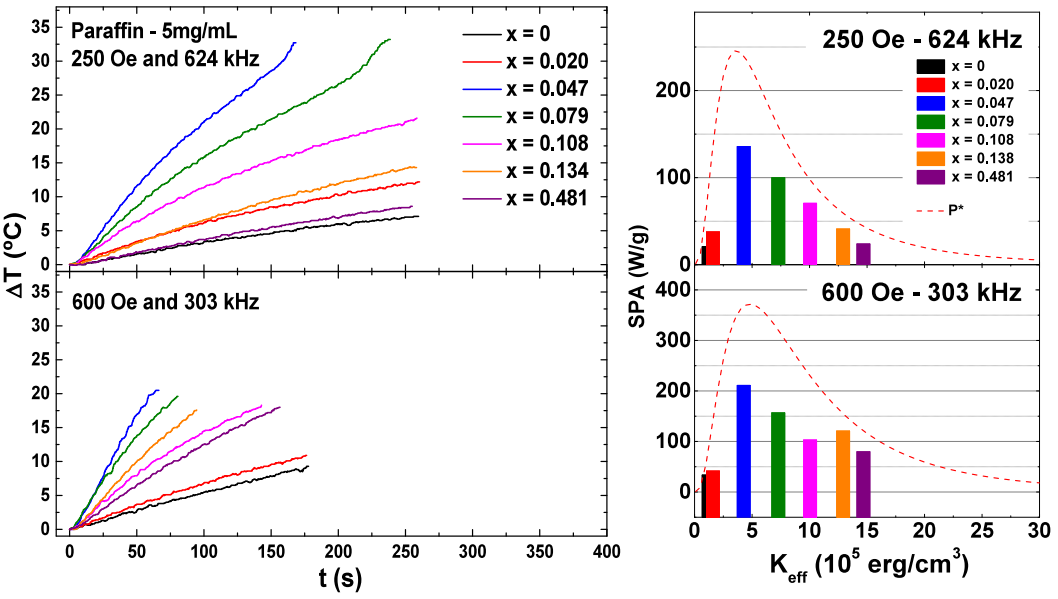

Figure 9. On the left side, representative MH experiments of $Co_xFe_{3-x}O_4$ MNPs dispersed in paraffin with concentration of 5 mg/mL and performed in the D5 series. On the right are their respective values of SPA as a function of K_{eff} obtained from $\frac{M_r(T)}{M_S}$ analysis. The red dashed lines are the calculated power dissipation P^*, assuming a size distribution.

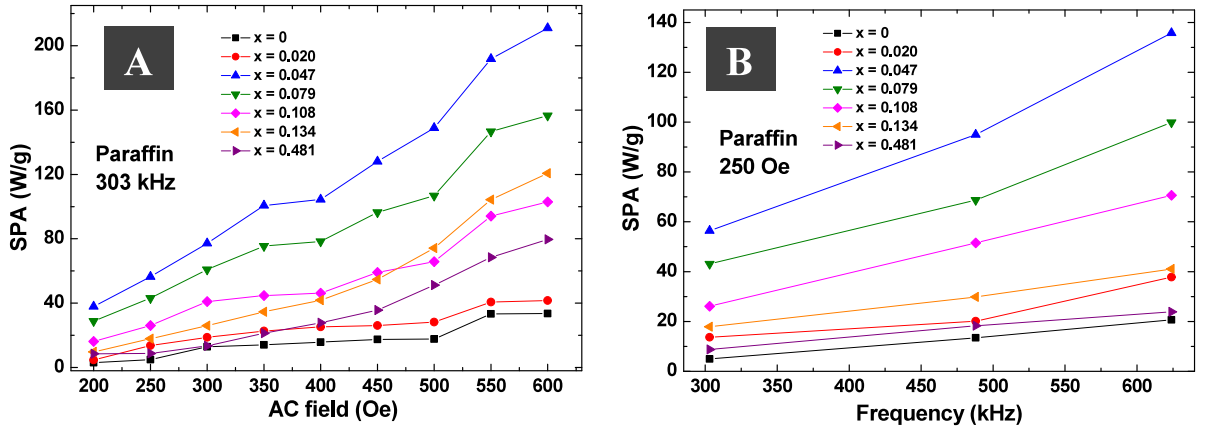

Figure 10. Experimental SPA of $Co_xFe_{3-x}O_4$ magnetic nanoparticles dispersed in paraffin with a concentration of 5 mg/mL and performed in D5 Series. (A) Obtained SPA for the frequency of 303 kHz as a function of the field amplitude and (B) SPA for a field amplitude of 250 Oe as a function of the frequency.

efficiency). Furthermore, notably, the substitution of Co led to a transition in the type of K_{eff} from uniaxial to cubic, further enhancing our control over the magnetic properties of the nanoparticles.

The identified sweet spot in Co concentration and anisotropy not only enhances SAR but also emphasizes the need for customization in nanoparticle properties to achieve targeted and efficient heat generation across diverse applications. This work significantly contributes to the ongoing endeavor to optimize magnetic nanoparticles for hyperthermia, providing valuable insights into the nuanced adjustments required to elevate heating performance.

Moreover, our observations shed light on the size-dependent Co concentration considerations, elucidating that smaller particle systems necessitate higher Co concentrations for maximizing SPA, while larger particle systems require a smaller amount of Co. This nuanced understanding adds a practical dimension to the broader context of tailoring magnetic properties for enhanced hyperthermia applications. In essence, our study underscores the imperative of fine-tuning magnetic properties and offers a valuable framework for advancing the field of magnetic hyperthermia through targeted nanoparticle design.

AUTHOR INFORMATION

Corresponding Authors

Adriele Aparecida de Almeida – *Instituto de Física "Gleb Wataghin" - Universidade de Campinas, 13083-859 São Paulo, Brazil;* orcid.org/0000-0002-8380-2767; Email: adriele.dryk@gmail.com

Diego Muraca – *Instituto de Física "Gleb Wataghin" - Universidade de Campinas, 13083-859 São Paulo, Brazil;* orcid.org/0000-0002-4530-4265; Email: dmuraca@unicamp.br

https://doi.org/10.1021/acsami.4c03343
ACS Appl. Mater. Interfaces XXXX, XXX, XXX−XXX

Authors

Fernando Fabris − *Instituto de Física "Gleb Wataghin" - Universidade de Campinas, 13083-859 São Paulo, Brazil;* orcid.org/0000-0003-3078-3811

Gustavo Soares da Silva − *Instituto de Física "Gleb Wataghin" - Universidade de Campinas, 13083-859 São Paulo, Brazil;* orcid.org/0000-0001-5550-5098

Kleber Roberto Pirota − *Instituto de Física "Gleb Wataghin" - Universidade de Campinas, 13083-859 São Paulo, Brazil;* orcid.org/0000-0002-1467-4415

Marcelo Knobel − *Instituto de Física "Gleb Wataghin" - Universidade de Campinas, 13083-859 São Paulo, Brazil;* orcid.org/0000-0002-6540-9267

Complete contact information is available at: https://pubs.acs.org/10.1021/acsami.4c03343

Funding

The Article Processing Charge for the publication of this research was funded by the Coordination for the Improvement of Higher Education Personnel - CAPES (ROR identifier: 00x0ma614).

Notes

The authors declare no competing financial interest.

■ ACKNOWLEDGMENTS

This study was mainly supported and performed under the auspices of the São Paulo research foundation (FAPESP) through Grant no. 2017/10581-1 and 2022/16460-0, CNPq 303227/2020-6, and 305057/2023-5. A.A.d.A. is the beneficiary of a postdoctoral FAPESP fellowship Grant no. 2021/13592-0. Futhermore, F.F. is the beneficiary of a postdoctoral FAPESP fellowship Grant no. 2019/13678-1. This research used facilities of the Brazilian Nanotechnology National Laboratory (LNNano), part of the Brazilian Centre for Research in Energy and Materials (CNPEM), a private nonprofit organization under the supervision of the Brazilian Ministry for Science, Technology, and Innovations (MCTI). The electronic microscopy staff is acknowledged for the assistance during the experiments (proposal numbers: 20210585 and 20230533).

■ REFERENCES

(1) Torres, T. E.; Lima, E., Jr; Calatayud, M. P.; Sanz, B.; Ibarra, A.; Fernández-Pacheco, R.; Mayoral, Á.; Marquina, C.; Ibarra, M. R.; Goya, G. F. The Relevance of Brownian Relaxation as Power Absorption Mechanism in Magnetic Hyperthermia. *Scientific Reports.* **2019**, *9* (1), 3992.

(2) Fernandes, S.; Fernandez, T.; Metze, S.; Balakrishnan, P. B.; Mai, B. T.; Conteh, J.; De Mei, C.; Turdo, A.; Di Franco, S.; Stassi, G.; Todaro, M.; Pellegrino, T. Magnetic Nanoparticle-Based Hyperthermia Mediates Drug Delivery and Impairs the Tumorigenic Capacity of Quiescent Colorectal Cancer Stem Cells. *ACS Applied Materials & Interfaces.* **2021**, *13* (14), 15959−15972.

(3) Mamani, J. B.; Marinho, B. S.; Rego, G. N. D. A.; Nucci, M. P.; Alvieri, F.; Santos, R. S. D.; Ferreira, J. V. M.; Oliveira, F. A.; Gamarra, L. F. Magnetic Hyperthermia Therapy in Glioblastoma Tumor On-a-Chip Model. *Einstein (São Paulo).* **2019**, *18*, eAO4954.

(4) Fabris, F.; Lohr, J.; Lima, E.; De Almeida, A. A.; Troiani, H. E.; Rodríguez, L. M.; Vásquez Mansilla, M.; Aguirre, M. H.; Goya, G. F.; Rinaldi, D.; Ghirri, A.; Peddis, D.; Fiorani, D.; Zysler, R. D.; De Biasi, E.; Winkler, E. L. Adjusting the Néel Relaxation Time of Fe3O4/ZnxCo1−xFe2O4 Sore/Shell Nanoparticles for Optimal Heat Generation in Magnetic Hyperthermia. *Nanotechnology.* **2021**, *32* (6), No. 065703.

(5) Darwish, M. S.; Kim, H.; Lee, H.; Ryu, C.; Lee, J. Y.; Yoon, J. Synthesis of Magnetic Ferrite Nanoparticles with High Hyperthermia Performance via a Controlled Co-Precipitation Method. *Nanomaterials.* **2019**, *9* (8), 1176.

(6) de Almeida, A. A.; De Biasi, E.; Mansilla, M. V.; Valdés, D. P.; Troiani, H. E.; Urretavizcaya, G.; Torres, T. E.; Rodríguez, L. M.; Fregenal, D. E.; Bernardi, G. C.; Winkler, E. L.; Goya, G. F.; Zysler, R. D.; Lima, E., Jr Magnetic Hyperthermia Experiments with Magnetic Nanoparticles in Clarified Butter Oil and Paraffin: a Thermodynamic Analysis. *J. Phys. Chem. C* **2020**, *124* (50), 27709−27721.

(7) Brollo, M. E.; Pinheiro, I. F.; Bassani, G. S.; Varet, G.; Merino-Garcia, D.; Guersoni, V. C.; Knobel, M.; Bannwart, A. C.; van der Geest, C.; Muraca, D. Iron Oxide Nanoparticles in a Dynamic Flux: Magnetic Hyperthermia Effect on Flowing Heavy Crude Oil. *ACS Omega.* **2023**, *8* (36), 32520−32525.

(8) Pinheiro, I. F.; Brollo, M. E.; Bassani, G. S.; Varet, G.; Merino-Garcia, D.; Guersoni, V. C.; Knobel, M.; Bannwart, A. C.; Muraca, D.; van der Geest, C. Effect of Viscosity and Colloidal Stability on the Magnetic Hyperthermia of Petroleum-Based Nanofluids. *Fuel.* **2023**, *331*, No. 125810.

(9) Sharifi, I.; Shokrollahi, H.; Amiri, S. Ferrite-Based Magnetic Nanofluids Used in Hyperthermia Applications. *Journal of Magnetism and Magnetic materials.* **2012**, *324* (6), 903−915.

(10) Beković, M.; Ban, I.; Drofenik, M.; Stergar, J. Magnetic Nanoparticles as Mediators for Magnetic Hyperthermia Therapy Applications: A Status Review. *Applied Sciences.* **2023**, *13* (17), 9548.

(11) Kolhatkar, A. G.; Jamison, A. C.; Litvinov, D.; Willson, R. C.; Lee, T. R. Tuning the Magnetic Properties of Nanoparticles. *International Journal of Molecular Sciences.* **2013**, *14* (8), 15977−16009.

(12) Fabris, F.; Lima, E.; De Biasi, E.; Troiani, H. E.; Vasquez Mansilla, M.; Torres, T. E.; Fernandez Pacheco, R.; Ibarra, M. R.; Goya, G. F.; Zysler, R. D.; Winkler, E. L. Controlling the Dominant Magnetic Relaxation Mechanisms for Magnetic Hyperthermia in Bimagnetic Core−Shell Nanoparticles. *Nanoscale.* **2019**, *11* (7), 3164−3172.

(13) Ali, A.; Shah, T.; Ullah, R.; Zhou, P.; Guo, M.; Ovais, M.; Tan, Z.; Rui, Y. Review on Recent Progress in Magnetic Nanoparticles: Synthesis, Characterization, and Diverse Applications. *Frontiers in Chemistry.* **2021**, *9*, No. 629054.

(14) Usov, N. A.; Liubimov, B. Y. Dynamics of Magnetic Nanoparticle in a Viscous Liquid: Application to Magnetic Nanoparticle Hyperthermia. *J. Appl. Phys.* **2012**, *112* (2), No. 023901.

(15) Rosensweig, R. E. Heating Magnetic Fluid with Alternating Magnetic Field. *Journal of Magnetism and Magnetic Materials.* **2002**, *252*, 370−374.

(16) Lima, E.; De Biasi, E.; Zysler, R. D.; Vasquez Mansilla, M.; Mojica-Pisciotti, M. L.; Torres, T. E.; Calatayud, M. P.; Marquina, C.; Ricardo Ibarra, M.; Goya, G. F. Relaxation Time Diagram for Identifying Heat Generation Mechanisms in Magnetic Fluid Hyperthermia. *Journal of Nanoparticle Research.* **2014**, *16*, 1−11.

(17) Carrey, J.; Mehdaoui, B.; Respaud, M. Simple Models for Dynamic Hysteresis Loop Calculations of Magnetic Single-Domain Nanoparticles: Application to Magnetic Hyperthermia Optimization. *J. Appl. Phys.* **2011**, *109* (8), No. 083921.

(18) Liu, X. L.; Fan, H. M.; Yi, J. B.; Yang, Y.; Choo, E. S. G.; Xue, J. M.; Fan, D. D.; Ding, J. Optimization of Surface Coating on Fe3O4 Nanoparticles for High Performance Magnetic Hyperthermia Agents. *Journal of Materials Chemistry.* **2012**, *22* (17), 8235−8244.

(19) Gutiérrez, L.; De la Cueva, L.; Moros, M.; Mazarío, E.; De Bernardo, S.; De la Fuente, J. M.; Morales, M. P.; Salas, G. Aggregation Effects on the Magnetic Properties of Iron Oxide Colloids. *Nanotechnology.* **2019**, *30* (11), 112001.

(20) Coral, D. F.; Mendoza Zélis, P.; de Sousa, M. E.; Muraca, D.; Lassalle, V.; Nicolás, P.; Ferreira, M. L.; Fernández van Raap, M. B. Quasi-Static Magnetic Measurements to Predict Specific Absorption Rates in Magnetic Fluid Hyperthermia Experiments. *J. Appl. Phys.* **2014**, *115* (4), No. 043907.

(21) Shaterabadi, Z.; Nabiyouni, G.; Soleymani, M. Correlation Between Effects of the Particle Size and Magnetic Field Strength on the Magnetic Hyperthermia Efficiency of Dextran-Coated Magnetite Nanoparticles. *Materials Science and Engineering: C* **2020**, *117*, No. 111274.
(22) Deatsch, A. E.; Evans, B. A. Heating Efficiency in Magnetic Nanoparticle Hyperthermia. *Journal of Magnetism and Magnetic Materials.* **2014**, *354*, 163−172.
(23) Mamiya, H.; Fukumoto, H.; Cuya Huaman, J. L.; Suzuki, K.; Miyamura, H.; Balachandran, J. Estimation of Magnetic Anisotropy of Individual Magnetite Nanoparticles for Magnetic Hyperthermia. *ACS Nano* **2020**, *14* (7), 8421−8432.
(24) Cullity, B. D.; Graham, C. D. *Introduction to Magnetic Materials*, 2th ed.; John Wiley & Sons, 2009.
(25) Bozorth, R. M.; Tilden, E. F.; Williams, A. J. Anisotropy and Magnetostriction of Some Ferrites. *Phys. Rev.* **1955**, *99* (6), No. 1788.
(26) Virden, A.; Wells, S.; O'Grady, K. Physical and Magnetic Properties of Highly Anisotropic Cobalt Ferrite Particles. *Journal of Magnetism and Magnetic Materials.* **2007**, *316* (2), e768−e771.
(27) Rondinone, A. J.; Samia, A. C.; Zhang, Z. J. Characterizing the Magnetic Anisotropy Constant of Spinel Cobalt Ferrite Nanoparticles. *Appl. Phys. Lett.* **2000**, *76* (24), 3624−3626.
(28) Fantechi, E.; Innocenti, C.; Albino, M.; Lottini, E.; Sangregorio, C. Influence of Cobalt Doping on the Hyperthermic Efficiency of Magnetite Nanoparticles. *Journal of Magnetism and Magnetic Materials.* **2015**, *380*, 365−371.
(29) Yasemian, A. R.; Almasi Kashi, M.; Ramazani, A. Exploring the Effect of Co Concentration on Magnetic Hyperthermia Properties of CoxFe3−xO4 Nanoparticles. *Materials Research Express.* **2020**, *7* (1), No. 016113.
(30) Phong, L. T. H.; Manh, D. H.; Nam, P. H.; Lam, V. D.; Khuyen, B. X.; Tung, B. S.; Bach, T. N.; Tung, D. K.; Phuc, N. X.; Hung, T. V.; Mai, T. L.; Phan, T.-L.; Phan, M. H. Structural, Magnetic and Hyperthermia Properties and their Correlation in Cobalt-Doped Magnetite Nanoparticles. *RSC Adv.* **2021**, *12* (2), 698−707.
(31) Santos, F. J.; Nieto de Castro, C. A.; Dymond, J. H.; Dalaouti, N. K.; Assael, M. J.; Nagashima, A. Standard Reference Data for the Viscosity of Toluene. *Journal of Physical and Chemical Reference Data.* **2006**, *35* (1), 1−8.
(32) Anton Paar: Viscosity of Paraffin Wax. https://wiki.anton-paar.com/en/paraffin-wax/ (accessed: 2024-02-09).
(33) Kloster, M.; de Almeida, A. A.; Muraca, D.; Marcovich, N. E.; Mosiewicki, M. A. Chitosan-based Magnetic Particles as Adsorbents for Anionic Contaminants. *Engineered Science* **2023**, *22*, 851.
(34) Holzwarth, U.; Gibson, N. The Scherrer Equation Versus the 'Debye-Scherrer Equation'. *Nature Nanotechnology.* **2011**, *6* (9), 534−534.
(35) Knobel, M.; Nunes, W. C.; Socolovsky, L. M.; De Biasi, E.; Vargas, J. M.; Denardin, J. C. Superparamagnetism and Other Magnetic Features in Granular Materials: a Review on Ideal and Real Systems. *Journal of Nanoscience and Nanotechnology.* **2008**, *8* (6), 2836−2857.
(36) Aquino, V. R. R.; Figueiredo, L. C.; Coaquira, J. A. H.; Sousa, M. H.; Bakuzis, A. F. Magnetic Interaction and Anisotropy Axes Arrangement in Nanoparticle Aggregates Can Enhance or Reduce the Effective Magnetic Anisotropy. *Journal of Magnetism and Magnetic Materials.* **2020**, *498*, No. 166170.
(37) Tancredi, P.; Rivas-Rojas, P. C.; Moscoso-Londoño, O.; Muraca, D.; Knobel, M.; Socolovsky, L. M. Significant Coercivity Enhancement at Low Temperatures in Magnetically Oriented Cobalt Ferrite Nanoparticles. *Appl. Phys. Lett.* **2019**, *115* (26), 263104.
(38) Tancredi, P.; Rivas-Rojas, P. C.; Moscoso-Londoño, O.; Muraca, D.; Knobel, M.; Socolovsky, L. M. Size and Doping Effects on the Improvement of the Low-Temperature Magnetic Properties of Magnetically Aligned Cobalt Ferrite Nanoparticles. *J. Alloys Compd.* **2022**, *894*, No. 162432.
(39) Aquino, R.; Depeyrot, J.; Sousa, M. H.; Tourinho, F. A.; Dubois, E.; Perzynski, R. Magnetization Temperature Dependence and Freezing of Surface Spins in Magnetic Fluids Based on Ferrite Nanoparticles. *Phys. Rev. B* **2005**, *72* (18), No. 184435.
(40) Kachkachi, H.; Ezzir, A.; Nogues, M.; Tronc, E. Surface Effects in Nanoparticles: Application to Maghemite-FeO. *European Physical Journal B* **2000**, *14*, 681−689.
(41) Shendruk, T. N.; Desautels, R. D.; Southern, B. W.; Van Lierop, J. The Effect of Surface Spin Disorder on the Magnetism of γ-Fe2O3 Nanoparticle Dispersions. *Nanotechnology.* **2007**, *18* (45), No. 455704.
(42) Stoner, E. C.; Wohlfarth, E. P. A Mechanism of Magnetic Hysteresis in Heterogeneous Alloys. Philosophical Transactions of the Royal Society of London. *Series A, Mathematical and Physical Sciences.* **1948**, *240* (826), 599−642.
(43) Kurtan, U.; Topkaya, R.; Baykal, A. Sol-Gel Auto-Combustion Synthesis of PVP/CoFe2O4 Nanocomposite and its Magnetic Characterization. *Mater. Res. Bull.* **2013**, *48* (11), 4889−4895.
(44) Kumar, Y.; Shirage, P. M. Highest Coercivity and Considerable Saturation Magnetization of CoFe2O4 Nanoparticles with Tunable Band Gap Prepared by Thermal Decomposition Approach. *J. Mater. Sci.* **2017**, *52*, 4840−4851.
(45) Fabris, F.; Tu, K. H.; Ross, C. A.; Nunes, W. C. Influence of Dipolar Interactions on the Magnetic Properties of Superparamagnetic Particle Systems. *J. Appl. Phys.* **2019**, *126* (17), 173905.
(46) Nunes, W. C.; Cebollada, F.; Knobel, M.; Zanchet, D. Effects of Dipolar Interactions on the Magnetic Properties of γ-Fe2O3 Nanoparticles in the Blocked State. *J. Appl. Phys.* **2006**, *99* (8), No. 08N705.

https://doi.org/10.1021/acsami.4c03343
ACS Appl. Mater. Interfaces XXXX, XXX, XXX−XXX